International Journal of Nanomedicine

Dovepress
Taylor & Francis Group

Open Access Full Text Article

ORIGINAL RESEARCH

# Biohybrids of Anoxia-Targeted Bacteria/MDPP for Enabling Targeted Synergistic Immunotherapy and Chemotherapy Against Breast Tumors

Tian Hu[1,*], Linsong Zhang[2,*], Yun Lu[1], Kang Xiong[1], Qian Wen[1], Jingrong Huang[1], Hongjun Deng[1], Kewei Xiang[1], Ping Zhou[3], Shaozhi Fu[1,4]

[1]Department of Oncology, the Affiliated Hospital of Southwest Medical University, Luzhou, Sichuan, 646000, People's Republic of China; [2]Department of Oncology, The Affiliated Traditional Chinese Medicine Hospital of Southwest Medical University, Luzhou, Sichuan, 646000, People's Republic of China; [3]Department of Radiology, the Affiliated Hospital of Southwest Medical University, Luzhou, Sichuan, 646000, People's Republic of China; [4]Nuclear Medicine and Molecular Imaging Key Laboratory of Sichuan Province, Luzhou, Sichuan, 646000, People's Republic of China

*These authors contributed equally to this work

Correspondence: Ping Zhou; Shaozhi Fu, Email zhouping1@126.com; shaozhifu513@163.com



**Background:** The hypoxic tumor microenvironment (TME) significantly impacts the effectiveness of various therapies on breast cancer. Conventional chemotherapeutic agents are unable to target hypoxic tumor tissue specifically, leading to reduced treatment efficacy and severe systemic toxicity. In order to improve drug targeting ability, we developed a bioactive biomotors system (MDPP@Bif) for chemoimmunotherapy against breast cancer. Utilizing the self-driving properties of the anaerobic *Bifidobacterium infantis* (*B. infantis*, Bif), both doxorubicin (DOX) and anti-programmed cell death protein ligand-1 (αPD-L1) antibody can be delivered simultaneously to tumor tissues to exert an anti-tumor effect on breast cancer.

**Methods:** The physicochemical properties of diverse nano-formulations were systematically characterized. In vitro anti-tumor efficacy of the MDPP@Bif biomotors was assessed through comprehensive biological evaluations, including 3-(4,5-dimethylthiazol-2-yl)-2,5-diphenyltetrazolium bromide (MTT) assays, live/dead staining, c cellular uptake analysis, apoptosis quantification, and wound healing assays to evaluate the in vitro anti-tumor activity of the MDPP@Bif biomotors. Furthermore, the therapeutic potential of the MDPP@Bif biohybrids was validated in vivo using a murine breast cancer model by monitoring of tumor growth kinetics, body weight fluctuations, and survival outcomes. Immunofluorescence staining was also used to further validate T-cells infiltration in the tumor tissues.

**Results:** The developed MDPP@Bif biomotors can actively colonize hypoxic tumor tissues through Bif's inherent targeting ability, releasing DOX to inhibit tumor growth. The released αPD-L1 antibody specifically binds to PD-L1, reducing immune escape and activating T cells. The concentration of DOX in tumor tissues of the MDPP@Bif group was 2.5 times higher than in tumors treated with free DOX, significantly prolonging the median survival of mice to 62 days and reducing the toxic side effects of DOX.

**Conclusion:** The novel bacteria-propelled biomotor MDPP@Bif shows great potential in treating solid tumors through synergistic chemotherapy and immunotherapy.

**Keywords:** anaerobic bacteria, mesoporous silica nanoparticles, doxorubicin, anti-PD-L1 antibody, breast cancer, chemoimmunotherapy

## Introduction

Breast cancer is the most common malignant tumor in women,[1,2] making the treatment methods a popular research topic. However, traditional chemotherapy drugs often have significant toxic side effects on normal tissues and organs because they do not specifically target tumor cells.[3] Recent studies have shown that tumor immunotherapy has significant potential, particularly when utilizing immune checkpoint inhibitors like anti-programmed death ligand 1 antibodies (anti-PD-L1 antibodies), which offer new hope to patients. However, clinical practice has revealed that using immunotherapy

Received: 1 January 2025
Accepted: 13 May 2025
Published: 27 May 2025

alone as the primary treatment method may result in low response rates and adverse side effects.[4,5] Therefore, although both chemotherapy and immunotherapy have demonstrated certain efficacy in treating tumors, each has its limitations. Consequently, comprehensive approaches to tumor treatment that combine multiple therapeutic strategies (such as chemotherapy with immunotherapy) are becoming increasingly prevalent in clinical management of malignant breast tumors.[6–8]

To enhance the targeting ability of therapeutic drugs, nanocarriers provide significant advantages for targeted drug delivery to tumors. Mesoporous silica nanoparticles (MSNs) with porous structures are ideal candidates for efficient drug loading.[9] Studies have shown that MSNs serve as promising drug carriers across various biomedical applications,[10] particularly in anti-tumor chemotherapy and immunotherapy.[11,12] Owing to their large specific surface area and tunable pore structure, MSNs are well-suited for delivering various chemotherapeutic drugs, including oxaliplatin, paclitaxel, and doxorubicin.[13–15] Additionally, MSNs exhibit high biocompatibility and provide diverse ligand modification options, ensuring their biosafety while enabling rapid drug release in acidic TMEs, thereby enhancing their therapeutic efficacy in cancer treatment.[16–18] Owing to their small size, nanomedicines can preferentially accumulate in tumors via the enhanced penetration and retention (EPR) effect or enhance the anti-tumor effect through active drug targeting to tumor tissues.[19,20] However, whereas the EPR effect has been validated in animal models, it remains unverified in human clinical studies. Furthermore, owing to multiple intra-tumoral biological barriers, most nanoparticles fail to accumulate within deep hypoxic zones requiring antitumor effect.[21,22] Therefore, achieving precise and efficient delivery to tumor tissues is essential for optimizing therapeutic outcomes.

Tumor hypoxia not only weakens the efficacy of drugs but may also adversely impact patient prognosis. Researchers have used the natural oxygen deficiency of anaerobic bacteria to deliver drugs to hypoxic areas of tumors.[23–25] Bifidobacterium infantis (B. infantis) is a probiotic that belongs to the actinobacteria family, is a Gram-positive, non-spore-forming microorganism that predominantly colonizes the gastrointestinal tract of infants. Notably, this bacterium demonstrates tumor-targeting capabilities through its ability to accumulate in solid tumors following intravascular administration. This phenomenon is attributed to its preferential colonization of hypoxic and immunosuppressive tumor microenvironments that support bacterial survival and proliferation.[26] Some studies have focused on targeting hypoxic areas of tumors using Bifidobacterium as a carrier.[27,28] These findings collectively suggest that this specialized anaerobic probiotic has effective targeting abilities towards tumor tissues, allowing for the delivery of anti-tumor drugs to hypoxic regions of tumors to be feasible.

In this study, as illustrated in Scheme 1, mesoporous MSNs were first synthesized to serve as nanocarriers for loading the chemotherapeutic agent doxorubicin (DOX). Subsequently, the DOX-loaded MSNs were functionalized with a polydopamine (PDA) coating and further conjugated with an immune checkpoint inhibitor (anti-PD-L1 antibody, αPD-L1), thereby constructing dual-drug co-loaded nanoparticle complexes designated as MDPP. Subsequently, we created a novel biohybrid called MDPP@Bif by utilizing the adhesive properties of PDA to attach the MDPP nanoparticles to the surface of Bifidobacterium infantis. In a mouse model of breast cancer, the MDPP@Bif biohybrid was able to actively accumulate in tumor tissue due to the self-driving effect of Bifidobacterium infantis. Within the tumor microenvironment, which is characterized by low pH and high levels of GSH, the PDA coating was cleaved, releasing αPD-L1 and DOX to achieve a combination of chemotherapy and immunotherapy. Consequently, the biohybrid MDPP@Bif shows significant potential for comprehensive treatment of malignant solid tumors.

# Materials and Methods

## Cell Lines, Animals, and Main Reagents

The 4T1 breast cancer and CT26 colorectal cancer cell lines were obtained from the Chinese Academy of Sciences Cell Bank (Shanghai, China). Female BALB/c mice were purchased from Chongqing Tengxin Biotechnology Co., Ltd. (Chongqing, China). Approval for animal experiments was obtained from the Animal Care and Ethics Committee of Southwest Medical University (License No. SWMU20230024). All animal experiments were conducted in compliance with the guidelines of the National Research Council's Guide for the Care and Use of Laboratory Animals. The mice (6-weeks old, weighing 16–18 g) were housed in a specific pathogen-free environment at 24°C, with 50% ~ 60% relative

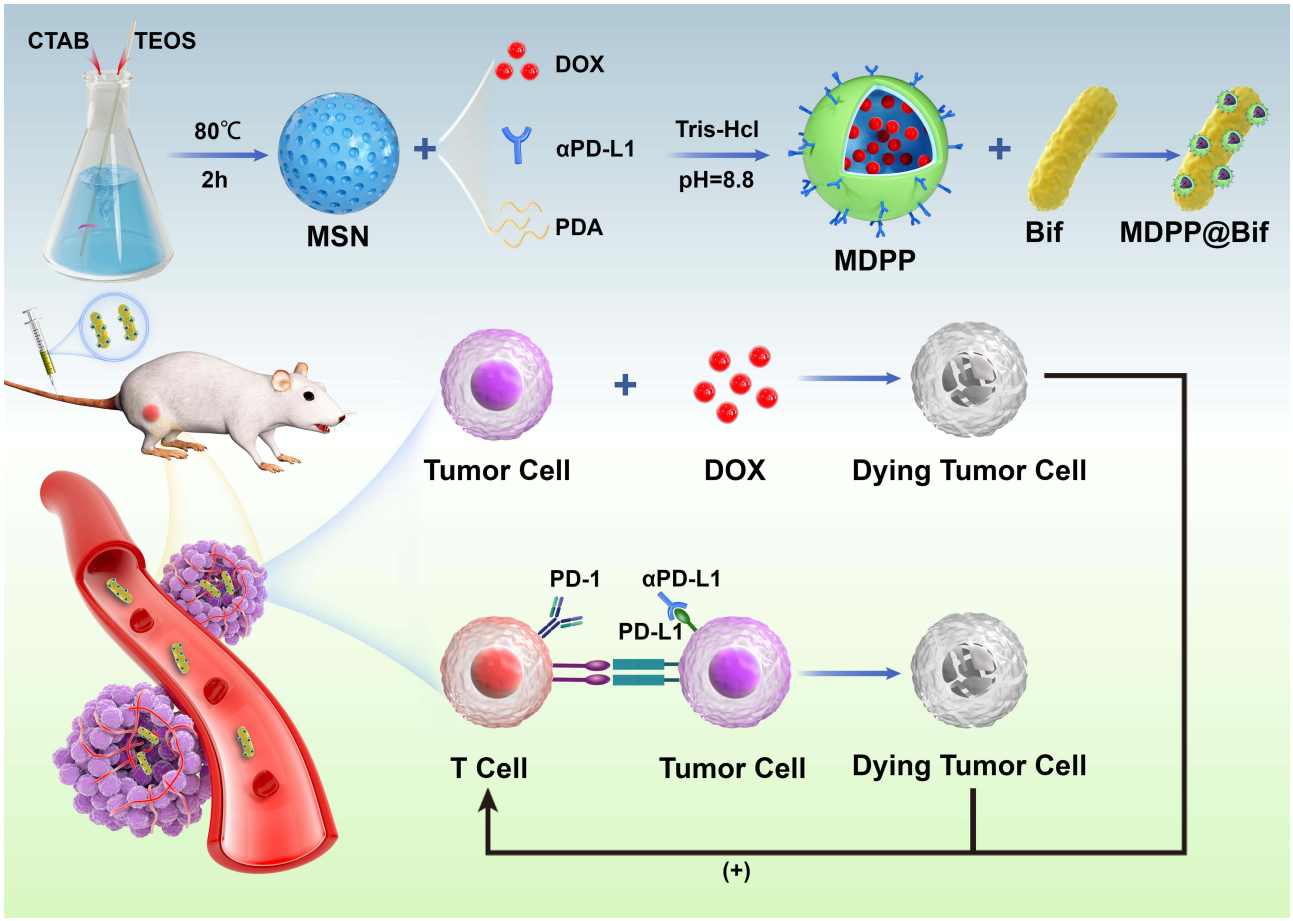


**Scheme 1** Schematic fabrication process of the bio-motor MDPP@Bif and its antitumor mechanism.

humidity, a 12-hour light/dark cycle, and provided standard food and tap water ad libitum. Throughout the experimental period, all mice remained healthy and showed no signs of infection. Tetraethyl orthosilicate (TEOS), cetyltrimethylammonium bromide (CTAB), and dopamine hydrochloride were purchased from Shanghai McLean Company Limited (Shanghai, China). The anti-PD-L1 antibody was obtained from Shenzhen BioXCell Company Limited (Shenzhen, China).

## Preparation and Characterization of MSNs

A 1.75 mL solution of NaOH (2 mol/L) was added to 240 mL of an aqueous cetyltrimethylammonium bromide (CTAB) solution. After stirring for 15 minutes at room temperature, 2.5 mL of tetraethyl orthosilicate (TEOS) was added to the mixture. The reaction was then stirred vigorously at 80°C for 2 h. Subsequently, the mixture was centrifuged at 3000 r/min for 30 min, the precipitates were washed three times with deionized water and anhydrous ethanol, filtered through a membrane, and lyophilized. The morphology of MSNs was observed by transmission electron microscopy (TEM, Tecnai G2 F30 S-TWIN, FEI, USA), and the particle size was determined using dynamic light scattering (DLS, NanoBrook 90Plus Zeta, Brookhaven Instrument, USA).

## Preparation and Characterization of MDP NPs

Ten milligrams of DOX was dissolved in 10 mL of Tris-HCl buffer solution (50 mm, pH 8.8). Next, 50 mg of MSNs was added and stirred for 24 h at room temperature. Subsequently, 25 mg of dopamine was dissolved in 40 mL of Tris buffer and mixed with the above dispersion, which was then stirred at 25°C for 12 h. To remove unloaded DOX, the product was collected by centrifugation and gently washed with Tris-buffer at a pH of 8.8. The drug loading (DL) and


https://doi.org/10.2147/IJN.S515213

encapsulation efficiency (EE) of DOX were calculated using an ultraviolet spectrophotometer (UV-5800pc, Shanghai Metash Instruments Co., Ltd, Shanghai, China). The in vitro stability of MDP NPs was then monitored in phosphate buffered saline (PBS), incomplete Dulbecco's modified Eagle's medium (DMEM), and fetal bovine serum (FBS) at 4°C, 25°C, and 37°C by measuring particle size changes. The physicochemical properties of the prepared MDP NPs were verified through thermogravimetric analysis (TGA), x-ray diffraction (XRD), zeta potential, and $N_2$ physisorption tests.

## Preparation and Characterization of MDPP@Bif Biohybrid

Bacteria Bif ($1.0 \times 10^7$ CFU) was cultured overnight at 37°C. The bacterial cells were then added to 5 mL of a 10 mm Tris-HCl buffer (pH 8.8) containing 10 mg of MDP nanoparticles and 2 mg of αPD-L1 antibody. After shaking at 100 rpm for 4 h at room temperature, the MDPP@Bif biohybrid was collected by centrifugation at 2700 rpm for 5 min and washed with 1×PBS to remove unconjugated αPD-L1 antibody. The successful modification of αPD-L1 antibody on the bacterial surface was verified using sodium dodecyl sulfate-polyacrylamide gel electrophoresis (SDS-PAGE). The morphology of the resulting MDPP@Bif biohybrids was observed using TEM and scanning electron microscopy (SEM, SU8020, Hitachi, Japan).

## In vitro Release of DOX

Samples containing the same dose of DOX were dissolved in PBS at different pH levels (5.0, 6.5, 7.4) and then placed into dialysis bags with a molecular-weight cutoff of 3500 Da. The bags were submerged in a shaking water bath set to 100 rpm. At predetermined time intervals, 5mL of the release medium was removed and replaced with fresh medium. The absorbance of the samples was measured at 485 nm using a UV spectrophotometer. The cumulative drug release profile was calculated and plotted.

## In vitro Cytotoxicity Assay

The 4T1 breast cancer cells were seeded in 96-well plates and treated with varying concentrations of the following drugs: MD NPs, MDP NPs, and MDP@Bif biohybrids for 24 h. To each well, 20 μL of MTT solution (5 mg/mL) was added and incubated for 1 h. The formazan crystals were dissolved with 150 μL of dimethyl sulfoxide (DMSO), and the absorbance was measured at 490 nm using a fluorescence microplate reader (FLUOstar Omega). The toxic effects of MDP@Bif on tumor cell lines (4T1 and CT26) and the cytotoxicity of the tested drugs (MSNs, DOX, MD NPs, MDP NPs, and MDP@Bif biohybrids) were also evaluated at different pH levels (pH 7.4 and 6.5).

## Apoptosis Assays

The 4T1 and CT26 cells were seeded in 6-well plates at a density of $5\times10^4$ cells per well and treated with the following drugs: MSNs, DOX, MD NPs, MDP NPs, MDP@Bif biohybrids for 24 h. After the addition of 194 μL of Annexin V-mCherry binding buffer, the apoptotic cells were stained with Annexin V-mCherry and SYTOX Green for 20 min. Apoptotic cells was detected by flow cytometry (BD FACSVerse, Piscataway, NJ, USA). Apoptosis was also evaluated using live/dead cell staining. Tumor cells were seeded into 6-well plates at a density of $1.2\times10^5$ cells per well, incubated overnight, and then co-cultured with fresh medium containing DOX, MD NPs, MDP NPs, or MDP@Bif biohybrids for 24 h. The cells were stained with calcein-acetoxymethylester (calcein-AM, 1 μg/mL) and propidium iodide (PI, 1 μg/mL) for 30 min and observed using an inverted fluorescence microscope (IX73, Olympus Corporation, Tokyo, Japan).

## In vitro Cell Migration Assay

The 4T1 cells were seeded into 6-well plates at a density of $5.0\times10^5$ cells per well. A cell monolayer was scratched horizontally with a sterile pipette tip to create a wound. After washing three times to remove displaced cells, fresh medium containing the following drugs: MSNs, DOX, MD NPs, MDP NPs, MDP@Bif biohybrids was added with 100 μg/mL DOX. Images of the wound area were captured using a light microscope (Olympus, CKX53, Tokyo, Japan) at 0, 12, and 24 hrs, respectively. The migration rate was calculated based on the percentage of wound coverage.

## In vitro Hemolysis Assay

An erythrocyte suspension (1 mL, 0.2% v/v) was mixed with 1 mL of normal saline (NS) containing MSNs, MD NPs, MDP NPs, MDPP NPs, and MDPP@Bif biohybrids, followed by incubation at 37°C for 4 h. Erythrocytes incubated in double-distilled water and NS were used as the positive and negative controls, respectively. After centrifugation at 3000 rpm for 6 min, the optical density (OD) of the supernatant was measured at 540 nm using a UV5800PC spectrophotometer. The hemolysis rate was calculated according to the formula:

$$\text{Hemolysis rate}(\%) = \frac{(\text{OD value of the experimental group} - \text{OD value of the saline group})}{(\text{OD value of the positive control group} - \text{OD value of the saline group})} \times 100\%$$

## Verify Targeting of MDPP@Bif in vitro

The anaerobic biological activities of Bif and MDPP@Bif biohybrids were assessed by simulating an in vitro hypoxic TME using a Transwell chamber. To create a hypoxic environment, 0.2 mL of Bif or MDPP@Bif suspension ($3.0\times10^8$ CFU/mL) was added to the upper compartment, while the lower compartment contained a glucose solution (0.4 mL, 0.5 KU), glucose oxidase (0.5 KU), and catalase (0.5 KU). The bacterial count in the lower compartment were determined after 2 hrs.

## In vivo Targeting of MCDP@Bif Biomotors

Breast cancer xenografts were established by subcutaneously injecting 4T1 cells into the right leg of BALB/c mice. When the tumor volume reached 50 $mm^3$, the mice were intravenously administered 0.1 mL of the MDPP@Bif suspension. The mice were euthanized on days 1, 4, and 7 post-injection, and the major organs (heart, liver, spleen, lungs, and kidneys) and tumors were removed. The tissues were ground, and the homogenates were plated onto anaerobic agar plates. Colonies was counted after anaerobic incubation at 37°C for 48 hrs.

## In vivo Anti-Tumor Activity

A mouse model of breast cancer was established by subcutaneously injecting 0.1 mL of a 4T1 cell suspension ($5.0\times10^6$ cells) into the right leg of female BALB/c mice. When the tumor volume reached 50–80 $mm^3$, fifty mice were randomly divided into five groups (n=10): (I) Control, (II) MP@Bif, (III) DOX+αPD-L1, (IV) MDPP, and (V) MDPP@Bif groups. According to treatment plan, DOX was administered intravenously at a dose of 6mg/kg every other day for one week. Tumor size and body weight were measured every two days (n=7). After 2 weeks of treatment, major organs (heart, liver, spleen, lung, kidney) and tumors were collected for hematoxylin and eosin (H&E) staining, Masson staining, Terminal deoxyribonucleotidyl transferase-mediated dUTP-digoxigenin nick end labeling (TUNEL) staining, and immunohistochemical analysis of Ki67, HIF-1α, CD4, and CD8 (n=3). To investigate the in vivo biodistribution of DOX, tumor-bearing mice were injected with DOX, MDP NPs, and MDPP@Bif biohybrids, respectively (n=3). 24 hours later, the major organs and tumors were collected, weighed, and homogenized using a tissue grinder. The homogenate from each tissue (heart 300 μL, liver 1500 μL, spleen 300 μL, lungs 500 μL, kidneys 1500 μL, tumor 1000 μL) was mixed with 3 mL of precipitant, centrifuged at 10,000 rpm for 10 min, and the supernatant was collected. The fluorescence intensity was measured at an excitation wavelength of 480 nm and an emission wavelength of 570 nm. The DOX concentration of the organs was calculated using a standard curve (n=3).

## Evaluation of Early Treatment Response

The early therapeutic response was assessed using 18F-fludeoxyglucose positron emission tomography/computed tomography (18F-FDG PET/CT) scanning (Siemens, Germany). The tumor-bearing mice were fasted for 6 h before being injected with 100–150 μCi of 18F-FDG via the tail vein. Thirty minutes later, the mice were anesthetized for whole-body PET/CT scanning in two-dimensional mode with parameters set at 80 kV, 500 mA, and 1.5 mm slice collimation. The PET/CT images were examined by two nuclear medicine physicians. Regions of interest (ROIs) were manually outlined on the tumor images, and the maximum standard uptake value (SUVmax) and mean standard uptake value (SUVmean) were calculated based on the hottest single pixel within the tumor (n=3).

## In vivo Fluorescence Imaging

A specific amount of indocyanine green (ICG, 5mg) was mixed with 5 mL of MDPP@Bif solution (1 mg/mL) in the dark at room temperature for 24 h to create ICG-labeled MDPP nanoparticles and MDPP@Bif biohybrids. The labeled drugs were collected by centrifugation and rinsed with deionized water. Once the tumor volume reached approximately 200 $mm^3$, mice were intravenously injected with 100 μL of free ICG, MDPP/ICG, or MDPP/ICG@Bif (equivalent to 1 mg/kg ICG). The mice were then imaged using a near-infrared fluorescence microimaging system (Series III 900/1700, NIROPTICS Suzhou, China) at 6, 12, and 24 h after injection. Subsequently, the mice were euthanized, and the tumors and major organs were removed and imaged using the same imaging system.

## Biosafety Analysis

Healthy Kunming mice were intravenously administered MDPP@Bif biohybrids at a dose of 6mg/kg every 2 days for a total of three times per week. The mice in the control group were administered the same volume of normal saline (NS). Blood samples were collected via the retro-orbital pathway at 14 days post-injection. Blood physiological and biochemical indicators were analyzed, including erythrocytes (RBC), leukocytes (WBC), platelets (PLT), hemoglobin (HGB), mean erythrocyte hemoglobin concentration (MCHC), erythrocyte specific volume (HCT), mean hemoglobin (MCH), mean corpuscular hematocrit (MCV), neutrophil count (NEU), alanine aminotransferase (ALT), aspartate aminotransferase (AST), urea (UREA), glucose (GLU), glomerular filtration rate (GFR), albumin (ALB), and total cholesterol (TC).

## Statistical Analysis

Quantitative data are presented as mean ± SD. Statistical significance between groups was determined using an unpaired Student's *t*-test, with a p-value of less than 0.05 considered to be statistically significant.

# Results

## Preparation and Characterization of MDPP@Bif Biomotors

The synthesized MSNs were spherical in shape (Figure 1Aa), while the MDP NPs were smooth and spherical in shape after loading DOX and PDA coating (Figure 1Ab). TEM (Figure 1Ac) and SEM (Figure 1Ad) images show the formation of MDPP@Bif biohybrids by adhering MDPP nanoparticles onto the surface of Bif. Elemental mapping confirms the presence of silicon in the MDPP@Bif biohybrids (Figure 1B). The average particle sizes of MSNs and MDP NPs were approximately 132.97 nm and 132.10 nm, respectively (Figure 1C). The drug loading (DL) and encapsulation efficiency (EE) of DOX in the MDP NPs were 10.78% and 91.6%, respectively.

The $N_2$ adsorption-desorption isothermal profile shown in Figure 1D indicated that the loading of DOX and PDA coating significantly decreased the specific surface area of MSNs from 209.35 $m^2/g$ to 2.61 $m^2/g$. The decrease in the specific surface area was attributed to the loading of DOX into the mesopores of MSNs and subsequent sealing by PDA. XRD spectra shown in Figure 2A revealed that the characteristic peaks of MSNs in the range of 18°-24° were maintained in the MDP NPs. The characteristic diffraction peak of MSNs at 43.6° could also be observed in MDP NPs. Furthermore, the UV-vis absorbance plots showed that MDP NPs had a strong absorbance at 485 nm, corresponding to DOX (Figure 2B). TGA results also indicated that MDP NPs exhibited greater mass reduction compared to the MD NPs and MSNs. (Figure 2C). SDS-PAGE (Figure 2D) analysis showed that the αPD-L1 antibody was successfully loaded onto the MDPP@Bif biohybrids. These results collectively confirmed the successful construction of the self-driving biomotors MDPP@Bif.

The drug release patterns shown in Figure 2E revealed that the free DOX preparation and MD NPs exhibited higher drug release rates of 84.9 ± 0.43% and 62.6 ± 2.23% at pH 7.4, respectively, while only 23.71 ± 1.01% of DOX was released from the MDP NPs within 24h. However, in acidic media (pH 6.5 and 5.0), the release of DOX from MDP NPs increased to 34.15±0.05% and 43.01±0.05%, respectively. As shown in Figure 2F, electronegative MSNs were transformed into positively charged MDP NPs due to the PDA coating. The in vitro stability of MDP NPs indicated that the particle size of MDP NPs did not fluctuate significantly over 24 hours at 25°C (Figure 2Gb) or 37°C (Figure 2Gc) in various media, including PBS, FBS, and incomplete DMEM.

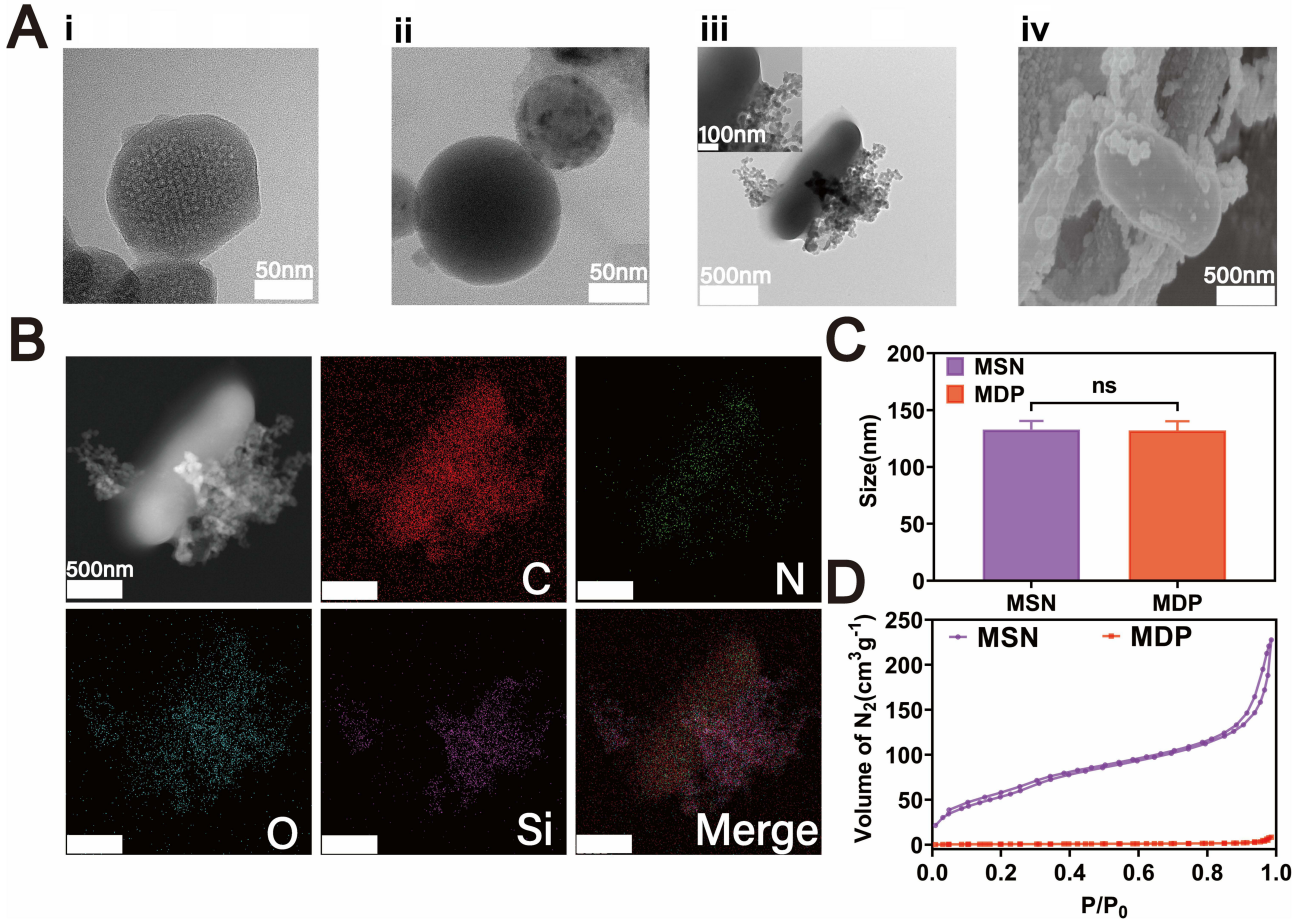


**Figure 1** In vitro characterization of MSN, MDP, MDPP@Bif. (**A**) TEM images of (i) MSN nanoparticles, (ii) MDP nanoparticles, (iii) biohybrid MDPP@Bif and SEM image of biohybrid MDPP@Bif (iv). (**B**) HAADF-STEM image and elemental mapping of biohybrid MDPP@Bif. (**C**) Mean particle size (n=3) of MSN and MDP. (**D**) $N_2$ adsorption-desorption curves of MSN and MDP.

## In vitro Anti-Tumor Efficacy of the MDP@Bif Hybrids

The cell viability of 4T1 cells was approximately 92.6% even when cultured with MSNs at a high dose of 1000 μg/mL (Figure 3A), indicating that MSNs were non-cytotoxic drug carriers. A similar result was obtained using CT26 cells (Figure S1). All DOX-based drugs exhibited concentration-dependent cytotoxicity on 4T1 cells, whether in neutral (pH 7.4, Figure 3B) or acidic (pH 6.5, Figure 3C) media. Additionally, at pH 6.5, cell viability significantly decreased from 43.4% to 24.3% after 4T1 cells were treated with 100 mg/mL of MDP NPs. The MDP NPs and MDP@Bif biohybrids both showed higher cytotoxicity at pH 6.5 due to the more release of DOX. The same results were obtained using CT26 cells (Figures S2 and S3). MDP@Bif had a similar cytotoxic effect with MDP NPs, indicating that attaching MDP NPs onto Bif did not affect its cytotoxicity. Live/dead staining was used to evaluate the toxic effects of various DOX formulations on 4T1 (Figure 3D) and CT26 cells (Figure S4). Almost no dead cells (red color) were detected in the control group, whereas a large number of dead cells were observed after treatment with DOX-containing drugs including free DOX, MD NPs, MDP NPs, and MDP@Bif biohybrids. Quantitative fluorescence intensity shown in Figure 3E also confirmed that MDP NPs and MDP@Bif had strong toxicity toward tumor cells. Furthermore, compared to free DOX, MD NPs and MDP NPs were easily absorbed by 4T1 cells (Figure 3F and G). Similar uptake was seen in CT26 cells (Figures S5 and S6). In line with this, the apoptosis rates of 4T1 cells treated with MDP NPs and MDP@Bif were 74.9% and 78.3%, respectively (Figure 4A), with no statistically significant difference compared to that induced by free DOX (77.32%, Figure 4B). Finally, scratch experiments showed that all DOX-containing drugs significantly inhibited 4T1 cell migration compared to the control. The healing rates of the MDP NPs (17.87%) and the MDP@Bif biohybrids (13.5%) were much smaller than that of the control group (78.56%) after 24 h (Figure 4C and D, $P<0.0001$).


https://doi.org/10.2147/IJN.S515213

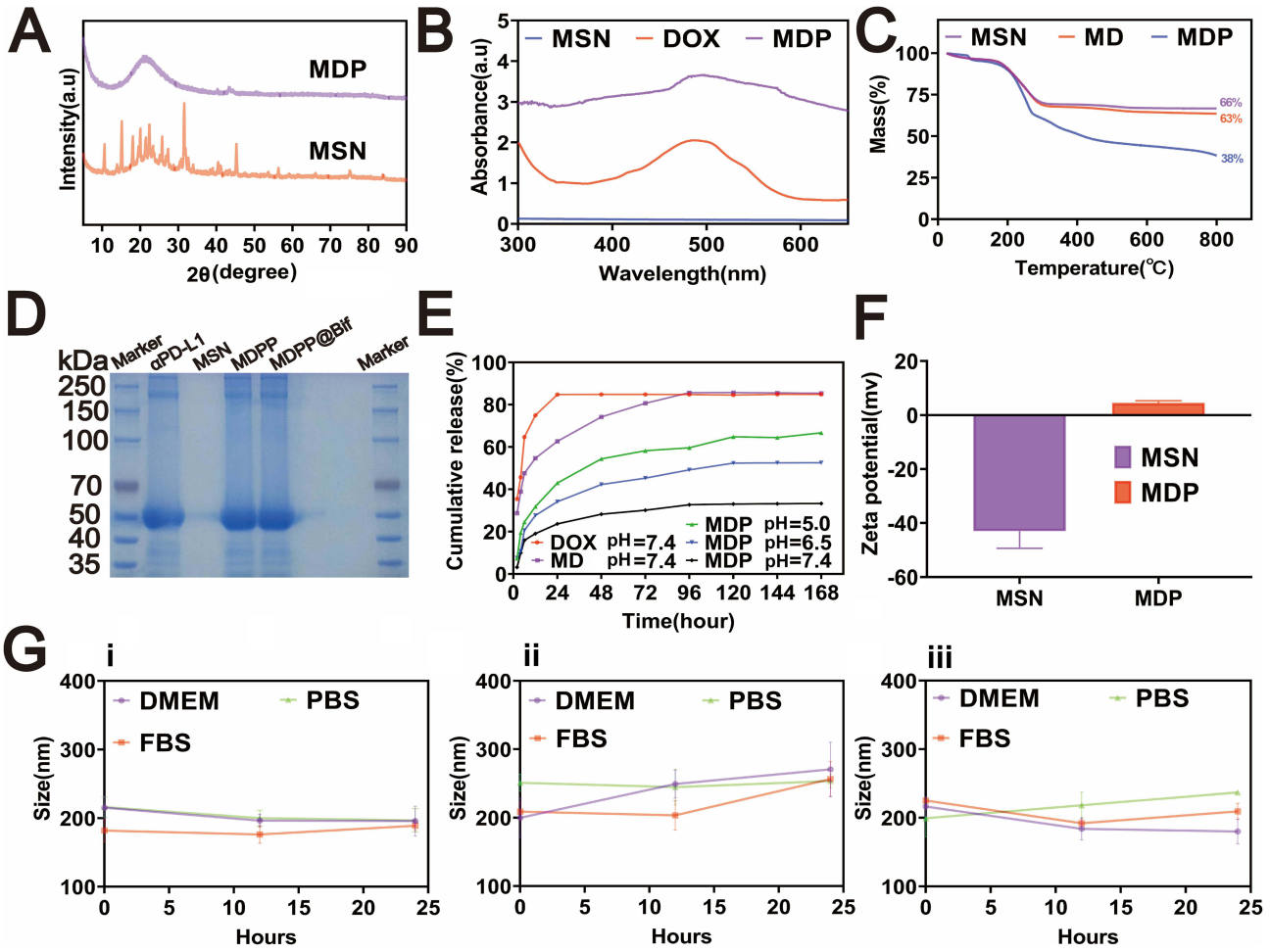


**Figure 2** Characterization of MDP, MDPP and MDPP@Bif. (**A**) XRD patterns of MSN, MDP nanoparticles. (**B**) UV-Vis absorption spectra of free DOX and MSN, MDP solution. (**C**) TGA curves of MSN, MD and MDP nanoparticles. (**D**) Protein analysis of αPD-L1, MSN, MDPP and MDPP@Bif. (**E**) In vitro release profiles of DOX, MD and MDP in PBS at PH of 5.0, 6.5 and 7.4. (**F**) zeta potential of MSN and MDP at the same concentration. (**G**) The change of particle size of MDP nanoparticles in DMEM, PBS and FBS at (i) 4°C, (ii) 25°C, and (iii) 37°C (n = 3, mean ± SD).

## The MDPP@Bif Biohybrid Selectively Localized to Hypoxic Tumor Zones

The biodistribution of MDPP@Bif biohybrids in tumors was illustrated in Figure 4E, revealing that the bacteria predominantly localized in the liver, kidney, and tumor. The number of bacteria present in the tumor tissue was notably greater than that in other organs (Figure 4F). By day 7 after injection, the bacteria in the liver and kidney had nearly disappeared, while the number of bacteria in the tumor tissue remained high ($P<0.001$). This suggests that MDPP@Bif did not diminish Bif's targeting ability for hypoxic tumors. To further confirm the targeting capability of MDPP@Bif, a hypoxic TME was simulated in the Transwell chamber using glucose oxidation-induced oxygen depletion, as shown in Figure 4G. The results demonstrated that the number of bacteria in the hypoxic chamber was significantly higher than that in the normoxic chamber after 2 h of incubation (Figure 4H).

## In vivo Anti-Tumor Effect of the MDPP@Bif Biohybrids

The early therapeutic response of MDPP@Bif biomotors on 4T1 tumor-bearing mice was evaluated using 18F-FDG PET/CT imaging. In Figure 5A, it can be seen that the MDPP@Bif treated mice had the lowest FDG uptake in tumor tissue compared to the other groups, in both lateral and longitudinal views. This is further supported by the fact that the MDPP@Bif group had the lowest SUVmax and SUVmean values among all the groups (Figure 5B and C), indicating a significant inhibition of glucose metabolism in the tumors. Additionally, the percentage of TUNEL-positive apoptotic cells in the MDPP@Bif group was higher compared to the other groups (Figure 5D–F), aligning with the enhanced anti-

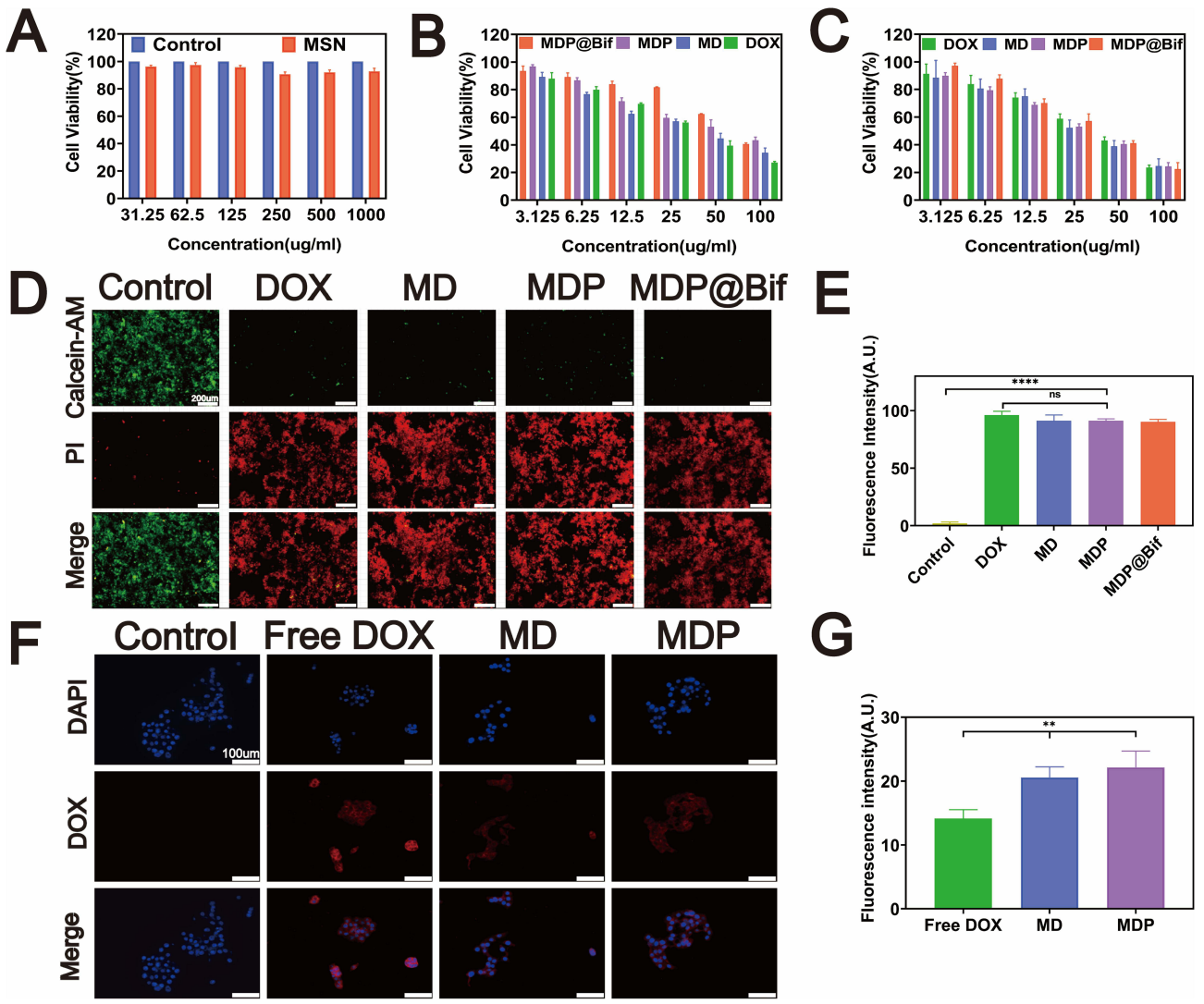


**Figure 3** In vitro cell experiments. (**A**) Cytotoxicity of MSN on 4T1 cells (n=6). Cytotoxicity assay of DOX, MD, MDP and MDP@Bif on 4T1 cells at pH of 7.4 (**B**) and 6.5 (**C**) (n = 3). (**D**) Live and dead cell staining of 4T1 cells treated with different drugs for 24 hours Calcein AM (green, live cells), PI (red, dead cells). (**E**) Quantification of PI fluorescence intensity in each group of 4T1 cells (n=3). (**F**) Fluorescence images of DOX, MD and MDP nanoparticles uptaken by 4T1 cells. (**G**) Quantitative analysis of fluorescence images of DOX, MD, and MDP nanoparticles uptake by 4T1 cells (n=3). (***P*<0.01, *****P*<0.0001).
**Abbreviation**: ns, no statistical significance.

tumor effect of MDPP@Bif biohybrids. Masson staining of myocardial tissues revealed significant myocardial fibrosis in the DOX+αPD-L1 group, likely due to the cardiotoxicity of DOX. In contrast, MDPP@Bif biohybrids showed reduced systemic toxicity to normal tissues because of its better targeting to tumor tissues (Figure 5E). Furthermore, according to the treatment process illustrated in Figure 6A, the MDPP@Bif-treated mice exhibited the smallest tumor volume and the slowest tumor growth rate (Figure 6B and E). The mice in the DOX+αPD-L1 group displayed symptoms such as wasting and poor mental status, likely due to the toxic side effects of DOX. Conversely, mice in the other treatment groups did not experience significant weight loss (Figure 6F). The enhanced anti-tumor effect of the MDPP@Bif treatment effectively prolonged the median survival time of mice to 62 days (Figure 6G). Immunohistochemical analysis of Ki-67 and HIF-1α expression indicated that the MDPP@Bif-treated mice significantly inhibited the proliferation of tumor cells and alleviated the hypoxia of tumor tissues (Figure 7A). In-situ expression of HIF-1α in the MDPP@Bif group was 21.3±1.51%, markedly lower than in the other groups (Figure 7B). Similarly, the MDPP@Bif group had the lowest percentage of Ki-67-positive cells (6.46±0.48%, Figure 7C). Moreover, the number of CD4+ and CD8+ T cells in the


https://doi.org/10.2147/IJN.S515213

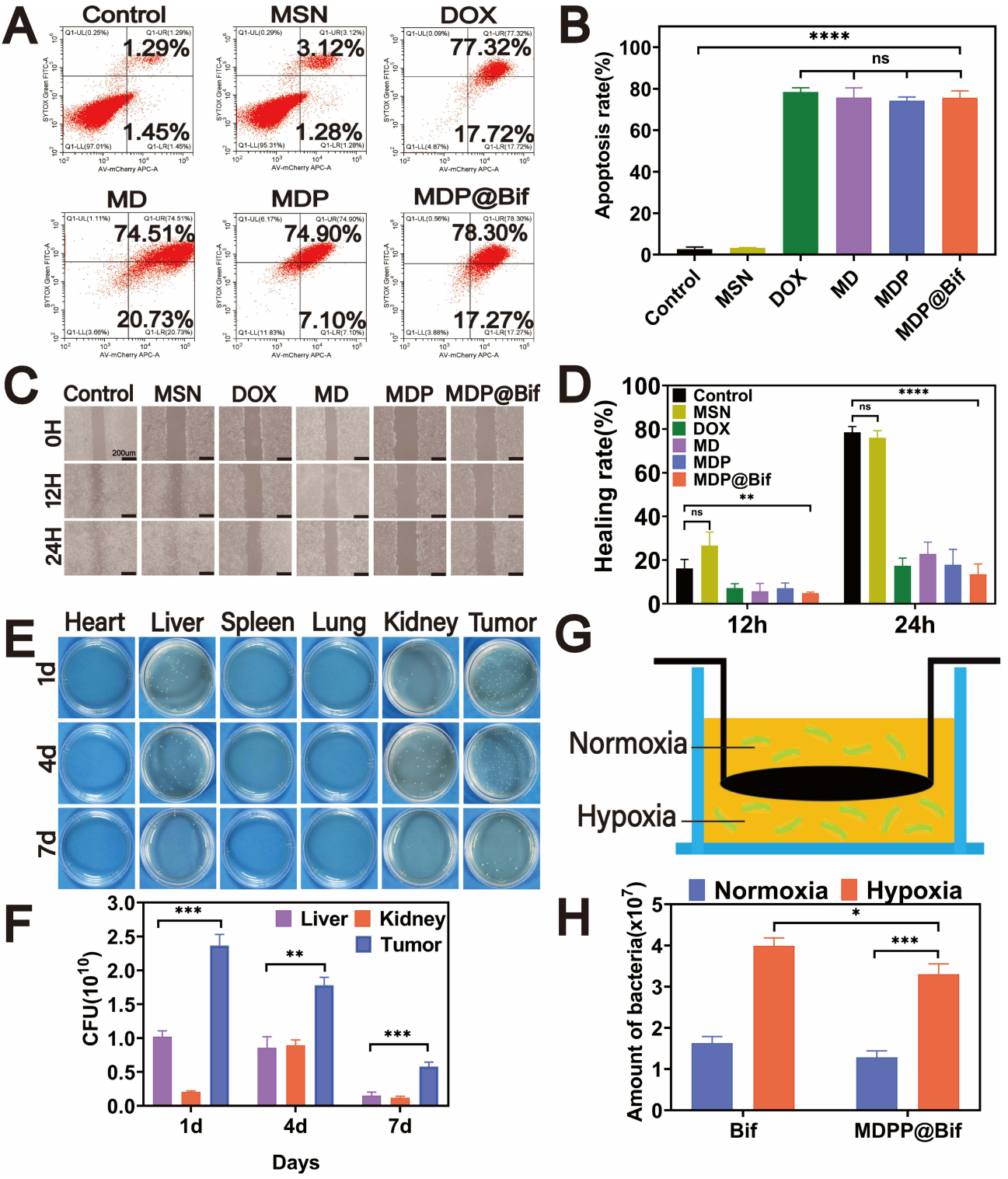


**Figure 4** In vitro cell experiments and evaluation of bioactivity and targeting ability of biomotor MDPP@Bif. (**A**) Flow cytometry analysis of 4T1 cells after co-incubation for 24 h. (**B**) Apoptosis rate in each group (n=3). (**C**) Photos of wound healing at 0, 12 and 24 hours. (**D**) Healing rate of each group (n=3). (**E**) Representative photographs of bacteria growth in heart, liver, spleen, lung, kidney and tumor tissue after injection of MDPP@Bif into 4T1 tumor-bearing mice on days 1, 4, and 7. (**F**) The number of Bif in liver, kidney and tumor after injection of MDPP@Bif (n=3). (**G**) Schematic diagram of a hypoxia model using the Transwell system to assess the chemotaxis of Bif and MDPP@Bif. (**H**) The number of bacteria in Transwell chambers (n=3). (*$P$<0.05, **$P$<0.01, ***$P$<0.001, ****$P$<0.0001).

**Abbreviation**: ns, no statistical significance.

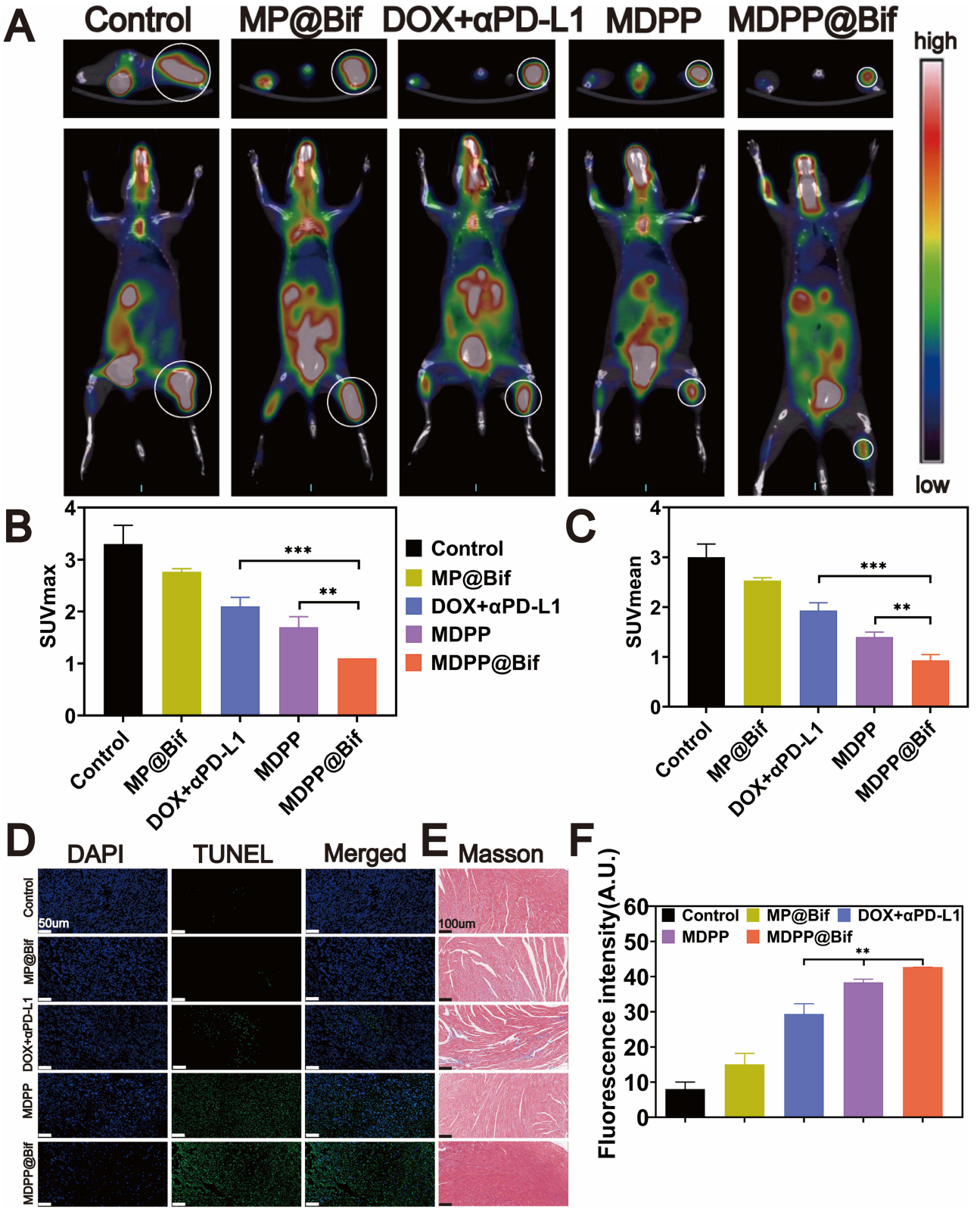


**Figure 5** In vivo treatment response in 4T1 tumor-bearing mice and in vivo evaluation of drug distribution. (**A**) Representative 18F-FDG PET/CT images of mice on day 12 of treatment, the upper layer: the cross-sectional images, the lower layer: the coronal images. White circles indicate tumor sites. (**B**) SUVmax of each group (n=3). (**C**) SUVmean of each group (n=3). (**D**) In vivo apoptosis of tumor tissue stained with DAPI and TUNEL on the 14th day of treatment, scale bar=50 μm. (**E**) Masson staining of heart in each group, scale bar =100 μm. (**F**) Quantitative fluorescence intensity of tumor tissue in each group by TUNEL analysis (n=3). (***P*<0.01, ****P*<0.001).


https://doi.org/10.2147/IJN.S515213

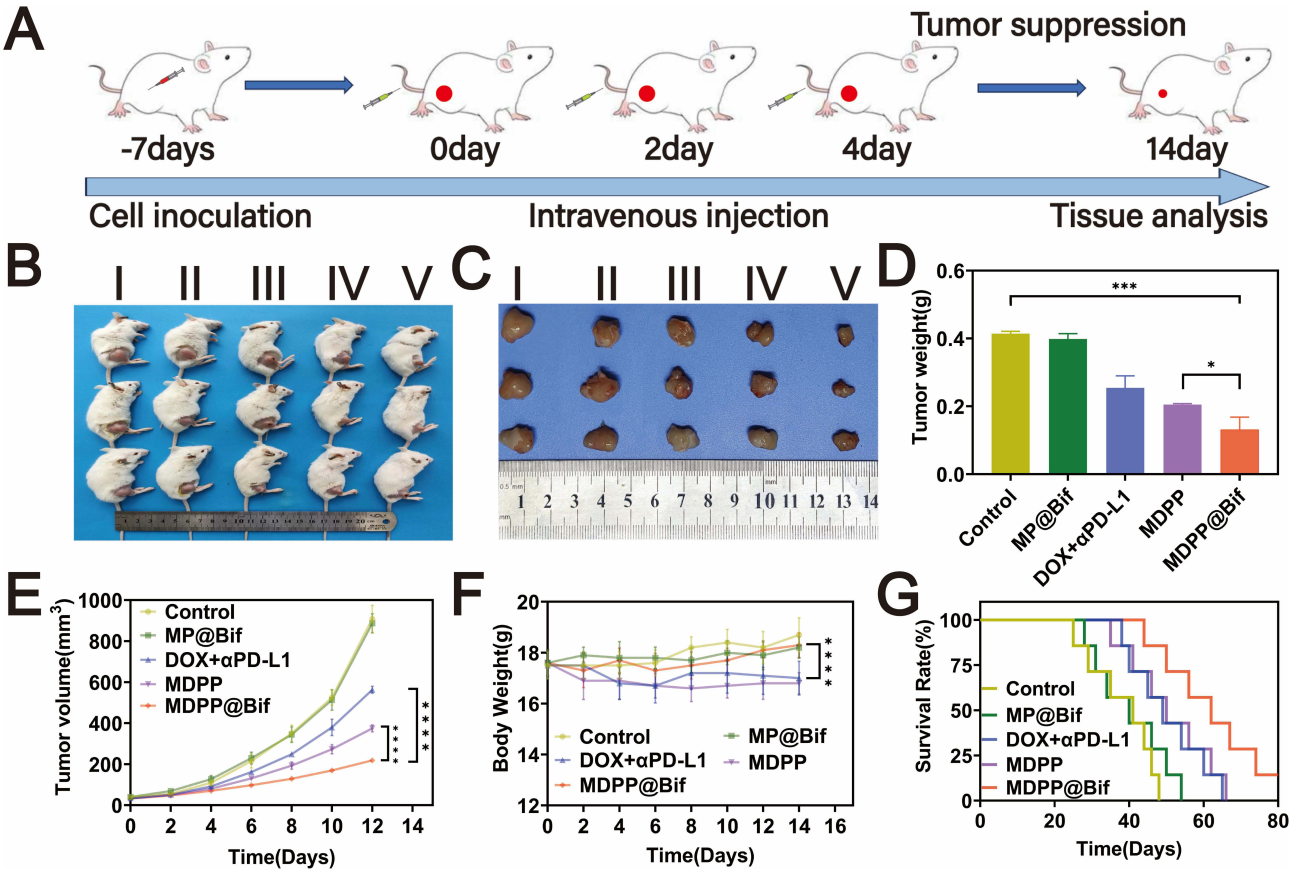


**Figure 6** In vivo evaluation of anti-tumor efficacy. (**A**) Schematic diagram of the treatment procedure. (**B**) Representative photographs of 4T1 tumor-bearing mice on the 14th day of treatment (n = 3), (I: Control, II: MP@Bif, III: DOX+αPD-L1, IV: MDPP, V: MDPP@Bif). (**C**) Representative photographs of isolated tumors (n = 3). (**D**) Weight of tumors (n=3). (**E**) Change in tumor volume (n=7). (**F**) Body weight fluctuations during treatment (n=7). (**G**) Survival curves of mice after treatments (n = 7). (**P*<0.05, ****P*<0.001, *****P*<0.000).

MDPP@Bif group was much higher than in the other groups, indicating that blocking the PD-L1 on the surface of tumor cells significantly increased the activation of immune cells (Figure 7D and E).

## In vivo Biodistribution of MDPP@Bif Biohybrids and Biosafety Assessment

ICG-labeled MDPP@Bif biohybrids were injected intravenously to investigate the in vivo biodistribution of bacteria-mediated biohybrids. As shown in Figure 8A, free ICG was gradually cleared over time, but a high accumulation of MDPP/ICG@Bif biohybrids was found in the tumor tissues at 24 h after injection, confirming the active targeting ability of self-propelled MDPP@Bif biomotors. Ex vivo imaging of tumor tissues at 24h also showed a strong fluorescent signal (Figure 8B). Furthermore, the intra-tumor concentration of DOX in the MDPP@Bif group was significantly higher than that in the other treatment groups, while relatively low drug levels were detected in major organs (Figure 8C, $P<0.001$). The biosafety of MDPP@Bif biohybrids was evaluated through in vitro hemolysis assay, H&E staining of major organs, and hematological analysis. No significant hemolysis was observed in tubes containing MSN, MD NPs, MDP NPs, MDPP NPs, or MDPP@Bif biohybrids (Figure S7). Typical photos of erythrocytes (Figure S7A), UV-visible absorption spectra (Figure S7B), and hemoglobin concentration (Figure S7C) also demonstrated good hemocompatibility of the MDPP@Bif biohybrids. Additionally, H&E staining of major organs (heart, liver, spleen, lungs, and kidneys) showed no significant tissue damage in all groups, except for some structural changes in the myocardium of DOX+αPD-L1-treated mice (Figure 8D). Hematological parameters and biochemical indicators were normal in all groups, with no significant toxic effect observed in the MDPP@Bif group compared to the control group (Figure S8).

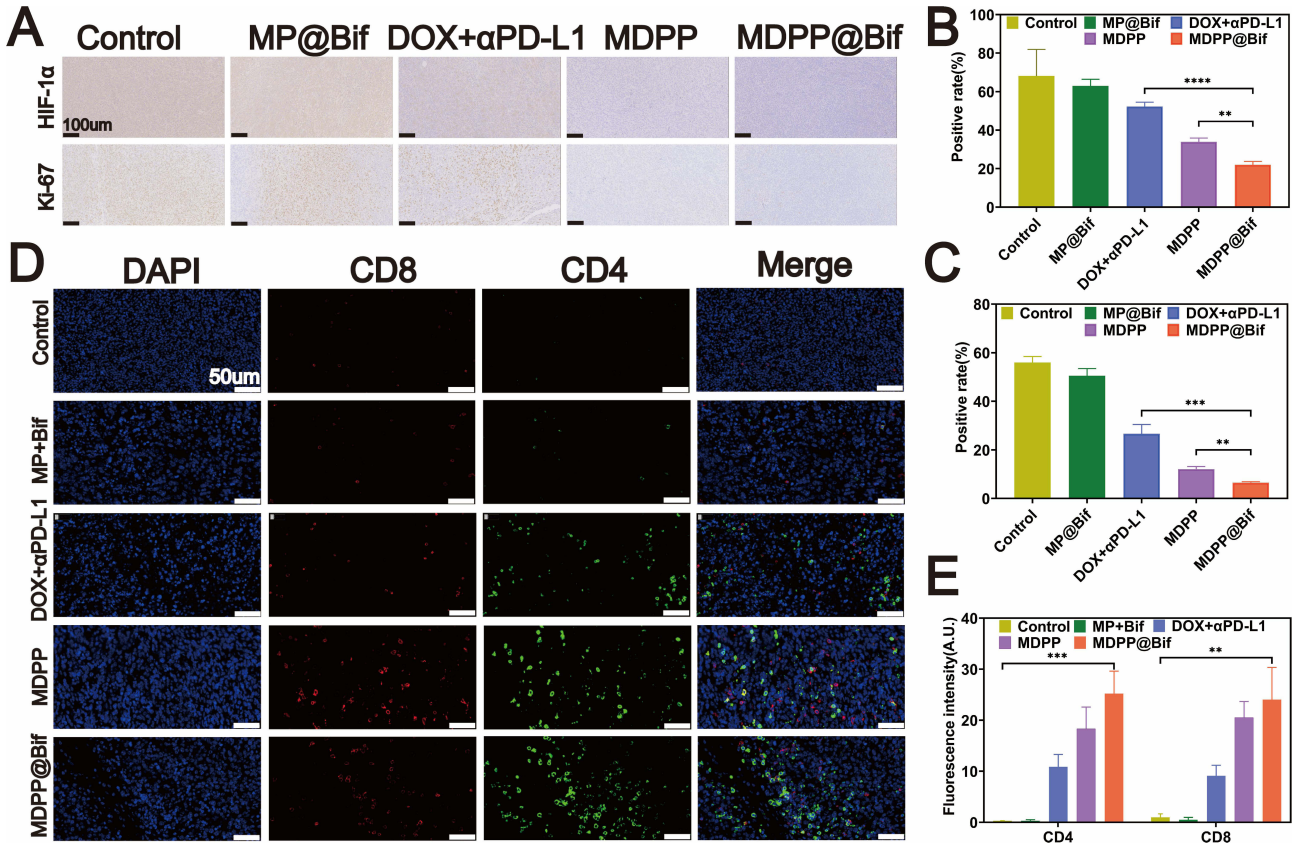


**Figure 7** In vivo evaluation of anti-tumor efficacy. (**A**) Micro-images of immunohistochemical staining on Ki67 and HIF-1α. Positive ratios of HIF-1α (**B**) and Ki67 (**C**), n=3. (**D**) Immunofluorescence images of CD4 and CD8 cells, scale bar = 50 μm. (**E**) Quantification of fluorescence intensity of CD4 and CD8 cells in each group (n=3) (***P*<0.01, ****P*<0.001, *****P*<0.0001).

## Discussion

To this day, the incidence of breast cancer remains high, posing a serious threat to women's lives, health, and safety. Studies have shown that the tumor microenvironment (TME) is characterized by low pH, high levels of glutathione (GSH), hypoxia, and inflammation, all of which promote the growth, proliferation, and metastasis of tumor cells.[29–31] Targeted tumor therapies can be developed based on these characteristics.[32–34] Research has demonstrated that leveraging these features of the TME can effectively inhibit tumor growth and improve clinical outcomes.[35–37] The hypoxic environment in tumors is primarily caused by abnormalities in the vascular system and blood supply,[38] which significantly impact the effectiveness of anticancer drugs.[39] Traditional chemotherapy drugs are unable to reach and accumulate in the hypoxic areas of solid tumors at high concentrations. Therefore, it is crucial to efficiently and accurately deliver therapeutic agents to hypoxic tumors to improve treatment efficacy.

Due to the natural properties of anaerobic bacteria, bacteria-mediated drug delivery systems have become a popular focus of research.[40,41] Song et al designed a microfluidic device to study how bacteria target hypoxic tumors through chemotaxis.[42] Kasinskas et al proposed that specific chemoreceptors, flagella, and signaling proteins are necessary for optimal bacterial aggregation at tumor sites.[43] Westphal et al argued that the immunosuppressive environment in tumors helps bacterial spread, and depleting neutrophils in the host further increases bacterial accumulation and spread.[44] Previous studies have shown that Bifidobacterium infantis (Bif) or its hybrids do not cause significant toxicity in mice after intravenous injection.[45,46] Zhang et al developed a self-guided biohybrid drug delivery system based on Bifidobacterium infantis, which can target tumor tissues and enhance the accumulation of chemotherapeutic drugs in hypoxic regions.[47] Xiao et al tested a thymidine kinase (BI-TK) suicide gene therapy system mediated by Bifidobacterium infantis, which effectively inhibited the growth of bladder tumors in rats.[48] In these drug formulations,


https://doi.org/10.2147/IJN.S515213

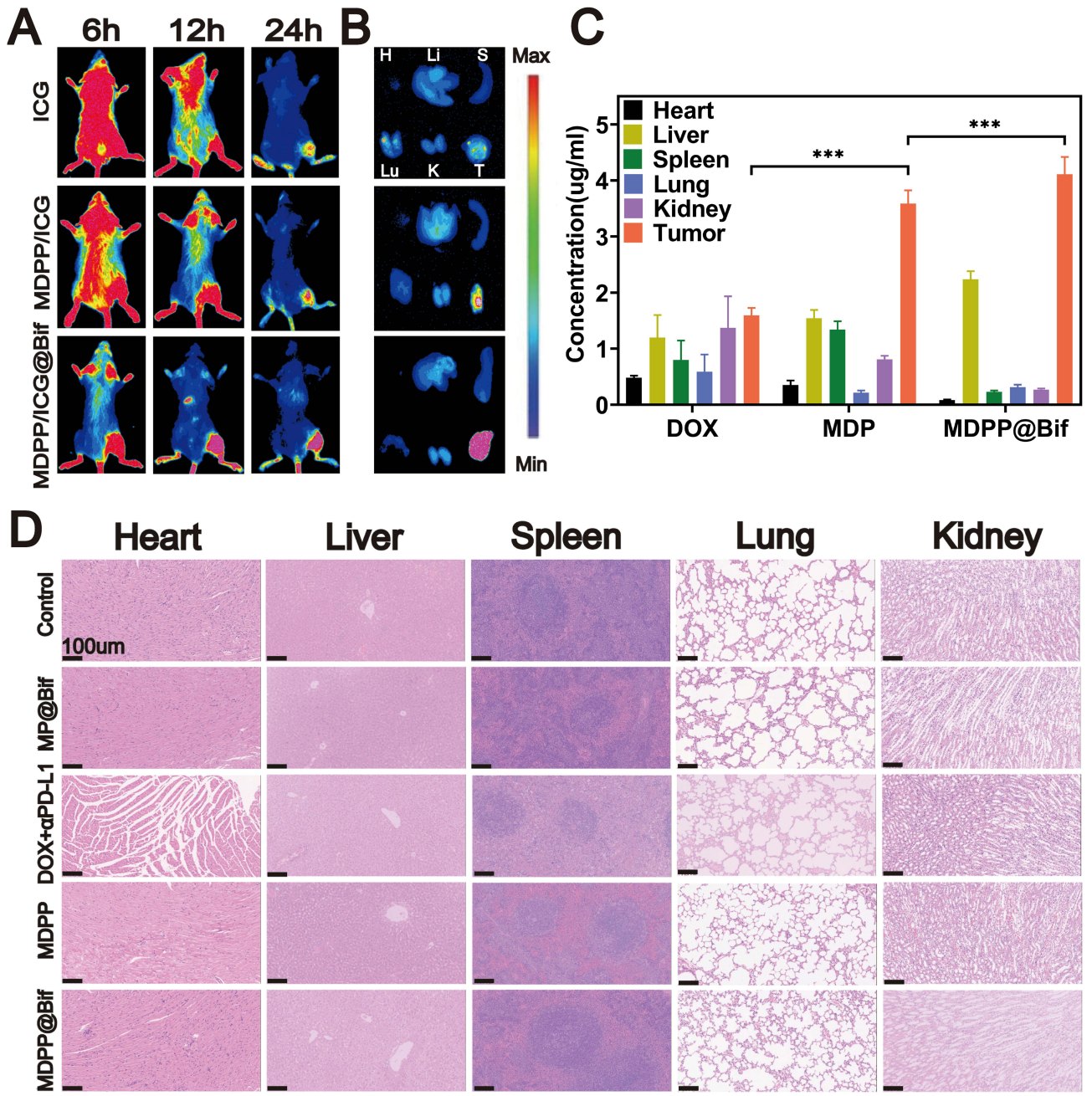


**Figure 8** In vivo evaluation of drug distribution. (**A**) fluorescence images of 4T1 tumor-bearing mice at different time points after intravenous injection of free ICG, MDPP/ICG and MDPP/ICG@Bif. (**B**) In vitro fluorescence images of isolated organs and tumors at 24 h of post-injection. (H: heart, Li: liver; S: spleen; Lu: lung, K: kidney, T: tumor). (**C**) In vivo distribution of DOX in organs and tumor (n=3). (**D**) H&E staining of major organs (heart, liver, spleen, lung, and kidney) after treatment as indicated, scale bar=100 μm. (***$P$<0.001).

the biological activity of Bifidobacterium infantis remained unchanged, and drugs were attached to the bacteria through chemical bonding,[49] electrostatic adsorption,[50] and antigen-antibody interactions.[51]

Consistent with previous studies, we observed a significant accumulation of Bifidobacterium infantis in the tumor tissues of a breast cancer mouse model after injecting MDPP@Bif biohybrids. This indicates that attaching MDPP nanoparticles to the surface of Bifidobacterium infantis does not reduce the bacteria's ability to target hypoxic regions of the tumor. Therefore, in this study, we utilized the anaerobic tropism of bacteria to simultaneously deliver the chemotherapeutic drug DOX and αPD-L1 antibody. We also innovatively used polydopamine (PDA) coating to modify MDPP nanoparticles. The use of PDA has three main advantages: First, the PDA coating contains various functional

groups, such as amino and hydroxyl groups, which can serve as binding sites for attaching the αPD-L1 antibody.[52–54] Second, the PDA coating acts as a switch to prevent the leakage of encapsulated doxorubicin (DOX). Third, the PDA coating itself is adhesive, which facilitates the binding of MDPP nanoparticles to Bifidobacterium infantis cells. Furthermore, the PDA coating may degrade in an acidic TME with high levels of GSH, selectively releasing DOX and αPD-L1 within tumors. This gradual release of DOX helps to maintain a high concentration of drug in tumor tissues while mitigating DOX-induced cardiotoxicity.[55] The released anti-PD-L1 antibody can bind to PD-L1 on tumor cells, preventing immune escape and promoting the activation of T cells,[56] proliferation,[57] and the production of tumor-killing cytokines.[58] Following treatment with MDPP@Bif biohybrids, the levels of CD4+ and CD8+ T cells in tumor tissues increased significantly. Overall, this biologically active MDPP@Bif hybrid has the ability to accumulate in tumor tissues and offer a synergistic chemo-immunotherapy effect, enhancing the anti-tumor response while reducing the systemic toxicity of DOX. Consequently, MDPP@Bif biohybrids hold potential as a therapeutic approach for breast cancer. However, further validation of the efficacy of this innovative bacteria-driven targeted drug delivery system is necessary in additional solid tumor models or in situ tumor models that more accurately replicate the actual tumor microenvironment.

## Conclusion

In this study, a new delivery system was developed, in which mesoporous silica nanoparticles (MSNs) containing doxorubicin (DOX) and αPD-L1 antibody were attached to the surfaces of Bifidobacterium infantis through polydopamine (PDA) coating. By utilizing the self-propelled movement of anaerobic bacteria, the biohybrids MDPP@Bif could target and accumulate in hypoxic tumors. The MDPP@Bif biohybrids released DOX in a pH-sensitive manner. In addition to the chemotherapy effects of DOX, αPD-L1-mediated immunomodulation increased the production of immune cells, such as CD4+ and CD8+ T cells, by blocking PD-L1 on the surfaces of tumor cells, thereby enhancing the immune response. Targeting hypoxia for delivery not only increased the concentration of DOX and αPD-L1 in tumor tissues, but also reduced their systemic toxicity. Therefore, the developed MDPP@Bif biohybrids can achieve synergistic therapeutic effects of chemo-immunotherapy on solid tumors.

## Funding

This study is supported by the Science and Technology Strategic Cooperation Programs of Luzhou Municipal People's Government and Southwest Medical University (2024LZXNYDJ017), the Project Program of the Science and Technology Department of Sichuan Province (2025ZNSFSC0679).

## Disclosure

The authors report no conflicts of interest in this work.

## References

1. Ferlay J, Soerjomataram I, Dikshit R, et al. Cancer incidence and mortality worldwide: sources, methods and major patterns in GLOBOCAN 2012. *Int J Cancer*. 2015;136(5):E359–86. doi:10.1002/ijc.29210
2. Torre LA, Bray F, Siegel RL, Ferlay J, Lortet-Tieulent J, Jemal A. Global cancer statistics, 2012. *CA Cancer J Clin*. 2015;65(2):87–108. doi:10.3322/caac.21262
3. Harbeck N, Ewer MS, De Laurentiis M, Suter TM, Ewer SM. Cardiovascular complications of conventional and targeted adjuvant breast cancer therapy. *Ann Oncol*. 2011;22(6):1250–1258. PMID: 21112929. doi:10.1093/annonc/mdq543
4. Emens LA. Breast Cancer Immunotherapy: facts and Hopes. *Clin Cancer Res*. 2018;24(3):511–520. PMID:28801472; PMCID: PMC5796849. doi:10.1158/1078-0432.CCR-16-3001
5. Tokumaru Y, Joyce D, Takabe K. Current status and limitations of immunotherapy for breast cancer. *Surgery*. 2020;167(3):628–630. PMID: 31623855; PMCID: PMC7028447. doi:10.1016/j.surg.2019.09.018
6. Cyprian FS, Akhtar S, Gatalica Z, Vranic S. Targeted immunotherapy with a checkpoint inhibitor in combination with chemotherapy: a new clinical paradigm in the treatment of triple-negative breast cancer. *Bosn J Basic Med Sci*. 2019;19(3):227–233. PMID: 30915922; PMCID: PMC6716092. doi:10.17305/bjbms.2019.4204
7. Gatti-Mays ME, Gameiro SR, Ozawa Y, et al. Improving the odds in advanced breast cancer with combination immunotherapy: stepwise addition of vaccine, immune checkpoint inhibitor, chemotherapy, and HDAC inhibitor in advanced stage breast cancer. *Front Oncol*. 2021;10:581801. PMID:33747894; PMCID: PMC7977003. doi:10.3389/fonc.2020.581801

8. Gebremeskel S, Lobert L, Tanner K, et al. Natural killer T-cell immunotherapy in combination with chemotherapy-induced immunogenic cell death targets metastatic breast cancer. *Cancer Immunol Res*. 2017;5(12):1086–1097. PMID: 29054890. doi:10.1158/2326-6066.CIR-17-0229
9. Manzano M, Vallet-Regi M. Mesoporous silica nanoparticles for drug delivery. *Adv Funct Mater*. 2020;30(2):1902634. doi:10.1002/adfm.201902634
10. Zou Y, Huang B, Cao L, Deng Y, Su J. Tailored mesoporous inorganic biomaterials: assembly, functionalization, and drug delivery engineering. *Adv Mater*. 2021;33(2):e2005215. PMID: 33251635. doi:10.1002/adma.202005215
11. Li X, Wang X, Ito A, Tsuji NM. A nanoscale metal organic frameworks-based vaccine synergises with PD-1 blockade to potentiate anti-tumour immunity. *Nat Commun*. 2020;11(1):3858. PMID: 32737343; PMCID: PMC7395732. doi:10.1038/s41467-020-17637-z
12. Li Z, Yang Y, Wei H, et al. Charge-reversal biodegradable MSNs for tumor synergetic chemo/photothermal and visualized therapy. *J Control Release*. 2021;338:719–730. PMID: 34509586. doi:10.1016/j.jconrel.2021.09.005
13. Wu Z, Li B, Qie Y, et al. Targeted inhibition of lymphovascular invasion formation with CREKA peptide-modified silicasomes to boost chemotherapy in bladder cancer. *Nano Lett*. 2024;24(33):10186–10195. PMID: 39136297. doi:10.1021/acs.nanolett.4c02485
14. Wu Y, Chang X, Yang G, et al. A physiologically responsive nanocomposite hydrogel for treatment of head and neck squamous cell carcinoma via proteolysis-targeting chimeras enhanced immunotherapy. *Adv Mater*. 2023;35(12):e2210787. PMID: 36656993. doi:10.1002/adma.202210787
15. Ho YJ, Wu CH, Jin QF, et al. Superhydrophobic drug-loaded mesoporous silica nanoparticles capped with β-cyclodextrin for ultrasound image-guided combined antivascular and chemo-sonodynamic therapy. *Biomaterials*. 2020;232:119723. PMID: 31891818. doi:10.1016/j.biomaterials.2019.119723
16. Zhang Z, Huang C, Zhang L, et al. pH-sensitive and bubble-generating mesoporous silica-based nanoparticles for enhanced tumor combination therapy. *Acta Pharm Sin B*. 2021;11(2):520–533. PMID: 33643828; PMCID: PMC7893139. doi:10.1016/j.apsb.2020.08.013
17. Zhou J, Yu Q, Song J, et al. Photothermally triggered copper payload release for cuproptosis-promoted cancer synergistic therapy. *Angew Chem Int Ed Engl*. 2023;62(12):e202213922. PMID: 36585379. doi:10.1002/anie.202213922
18. Zheng Q, Zou T, Wang W, et al. Necroptosis-mediated synergistic photodynamic and glutamine-metabolic therapy enabled by a biomimetic targeting nanosystem for cholangiocarcinoma. *Adv Sci*. 2024;11(29):e2309203. PMID: 38837691; PMCID: PMC11304281. doi:10.1002/advs.202309203
19. Chen ZA, Wu CH, Wu SH, et al. Receptor ligand-free mesoporous silica nanoparticles: a streamlined strategy for targeted drug delivery across the blood-brain barrier. *ACS Nano*. 2024;18(20):12716–12736. PMID: 38718220; PMCID: PMC11112986. doi:10.1021/acsnano.3c08993
20. Liu H, Han J, Lv Y, et al. Isorhamnetin and anti-PD-L1 antibody dual-functional mesoporous silica nanoparticles improve tumor immune microenvironment and inhibit YY1-mediated tumor progression. *J Nanobiotechnol*. 2023;21(1):208. PMID: 37408047; PMCID: PMC10321013. doi:10.1186/s12951-023-01967-3
21. Wang J, Zhou T, Liu Y, Chen S, Yu Z. Application of nanoparticles in the treatment of lung cancer with emphasis on receptors. *Front Pharmacol*. 2022;12:781425. doi:10.3389/fphar.2021.781425
22. Saggar JK, Yu M, Tan Q, Tannock IF. The tumor microenvironment and strategies to improve drug distribution. *Front Oncol*. 2013;3:154. doi:10.3389/fonc.2013.00154
23. Cronin M, Morrissey D, Rajendran S, et al. Orally administered Bifidobacteria as vehicles for delivery of agents to systemic tumors. *Mol Ther*. 2010;18(7):1397–1407. doi:10.1038/mt.2010.59
24. Fan J-X, Li Z-H, Liu X-H, et al. Bacteria-mediated tumor therapy utilizing photothermally-controlled TNF-α expression via oral administration. *Nano Lett*. 2018;18(4):2373–2380. doi:10.1021/acs.nanolett.7b05323
25. Chen Q, Bai H, Wu W, et al. Bioengineering bacterial vesicle-coated polymeric nanomedicine for enhanced cancer immunotherapy and metastasis prevention. *Nano Lett*. 2020;20:11–21. doi:10.1021/acs.nanolett.9b02182
26. Lu D, Wang L, Wang L, et al. Probiotic engineering and targeted sonoimmuno-therapy augmented by STING agonist. *Adv Sci*. 2022;9(22):e2201711. doi:10.1002/advs.202201711
27. Sasaki T, Fujimori M, Hamaji Y, et al. Genetically engineered bifidobacterium longum for tumor-targeting enzyme-prodrug therapy of autochthonous mammary tumors in rats. *Cancer Sci*. 2006;97(7):649–657.
28. Ngo N, Choucair K, Creeden JF, et al. Bifidobacterium SPP: the promising Trojan Horse in the era of precision oncology. *Future Oncol*. 2019;15(33):3861–3876. doi:10.2217/fon-2019-0374
29. Lee YC, Lam HM, Rosser C, Theodorescu D, Parks WC, Chan KS. The dynamic roles of the bladder tumour microenvironment. *Nat Rev Urol*. 2022;19(9):515–533. PMID: 35764795; PMCID: PMC10112172. doi:10.1038/s41585-022-00608-y
30. Clara JA, Monge C, Yang Y, Takebe N. Targeting signalling pathways and the immune microenvironment of cancer stem cells - a clinical update. *Nat Rev Clin Oncol*. 2020;17(4):204–232. PMID: 31792354. doi:10.1038/s41571-019-0293-2
31. Jin M-Z, Jin W-L. The updated landscape of tumor microenvironment and drug repurposing. *Signal Transduct Target Ther*. 2020;5(1):166. PMID: 32843638; PMCID: PMC7447642. doi:10.1038/s41392-020-00280-x
32. Chen B, Sang Y, Song X, et al. Exosomal miR-500a-5p derived from cancer-associated fibroblasts promotes breast cancer cell proliferation and metastasis through targeting USP28. *Theranostics*. 2021;11(8):3932–3947. PMID: 33664871; PMCID: PMC7914354. doi:10.7150/thno.53412
33. Yin H, Zhang X, Yang P, et al. RNA m6A methylation orchestrates cancer growth and metastasis via macrophage reprogramming. *Nat Commun*. 2021;12(1):1394. PMID: 33654093; PMCID: PMC7925544. doi:10.1038/s41467-021-21514-8
34. Xia X, Zhang Z, Zhu C, et al. Neutrophil extracellular traps promote metastasis in gastric cancer patients with postoperative abdominal infectious complications. *Nat Commun*. 2022;13(1):1017. PMID: 35197446; PMCID: PMC8866499. doi:10.1038/s41467-022-28492-5
35. Kobayashi H, Gieniec KA, Lannagan TRM, et al. The origin and contribution of cancer-associated fibroblasts in colorectal carcinogenesis. *Gastroenterology*. 2022;162(3):890–906. PMID: 34883119; PMCID: PMC8881386. doi:10.1053/j.gastro.2021.11.037
36. Li Z, Xu W, Yang J, et al. A tumor microenvironments-adapted polypeptide hydrogel/nanogel composite Boosts antitumor molecularly targeted inhibition and immunoactivation. *Adv Mater*. 2022;34(21):e2200449. PMID: 35291052. doi:10.1002/adma.202200449
37. Zhao Z, Qin J, Qian Y, et al. FFAR2 expressing myeloid-derived suppressor cells drive cancer immunoevasion. *J Hematol Oncol*. 2024;17(1):9. PMID: 38402237; PMCID: PMC10894476. doi:10.1186/s13045-024-01529-6
38. Goel S, Duda DG, Xu L, et al. Normalization of the vasculature for treatment of cancer and other diseases. *Physiol Rev*. 2011;91(3):1071–1121. Erratum in: Physiol Rev. 2014;94(2):707. PMID: 21742796; PMCID: PMC3258432. doi:10.1152/physrev.00038.2010

39. Nicolas-Boluda A, Silva AKA, Fournel S, Gazeau F. Physical oncology: new targets for nanomedicine. *Biomaterials*. 2018;150:87–99. PMID: 29035739. doi:10.1016/j.biomaterials.2017.10.014
40. Lin D, Feng X, Mai B, et al. Bacterial-based cancer therapy: an emerging toolbox for targeted drug/gene delivery. *Biomaterials*. 2021;277:121124. PMID: 34534860. doi:10.1016/j.biomaterials.2021.121124
41. Xiao Y, Pan T, Da W, et al. Aptamer-drug conjugates-loaded bacteria for pancreatic cancer synergistic therapy. *Signal Transduct Target Ther*. 2024;9(1):272. PMID: 39397032; PMCID: PMC11471780. doi:10.1038/s41392-024-01973-3
42. Song J, Zhang Y, Zhang C, et al. A microfluidic device for studying chemotaxis mechanism of bacterial cancer targeting. *Sci Rep*. 2018;8(1):6394. doi:10.1038/s41598-018-24748-7
43. Kasinskas RW, Forbes NS. Salmonella typhimurium lacking ribose chemoreceptors localize in tumor quiescence and induce apoptosis, Canc. *Res*. 2007;67(7):3201–3209. doi:10.1158/0008-5472.CAN-06-2618
44. Westphal K, Leschner S, Jablonska J, Loessner H, Weiss S. Containment of tumor-colonizing bacteria by host neutrophils, Canc. *Res*. 2008;68 (8):2952–2960. doi:10.1158/0008-5472.CAN-07-2984
45. Zhang R, Feng L, Dong Z, et al. Glucose & oxygen exhausting liposomes for combined cancer starvation and hypoxia-activated therapy. *Biomaterials*. 2018;162123–162131.
46. Tang Y, Chen C, Jiang B, et al. Bifidobacterium bifidum-mediated specific delivery of nanoparticles for tumor therapy. *Int J Nanomed*. 2021:164643–164659.
47. Zhang H, Wang Y, Li M, et al. A self-guidance biological hybrid drug delivery system driven by anaerobes to inhibit the proliferation and metastasis of colon cancer. *Asian J Pharm Sci*. 2022;17(6):892–907. PMID: 36600894; PMCID: PMC9800957. doi:10.1016/j.ajps.2022.09.003
48. Tang W, He Y, Zhou S, Ma Y, Liu G. A novel Bifidobacterium infantis-mediated TK/GCV suicide gene therapy system exhibits antitumor activity in a rat model of bladder cancer. *J Exp Clin Cancer Res*. 2009;28(1):155. PMID: 20015348; PMCID: PMC2803447. doi:10.1186/1756-9966-28-155
49. Fan J-X, Peng M-Y, Wang H, et al. Engineered bacterial bioreactor for tumor therapy via Fenton-like reaction with localized H(2) O(2) generation. *Adv Mater*. 2019;31(16):e1808278. doi:10.1002/adma.201808278
50. Zhang W, Liu J, Li X, et al. Precise chemodynamic therapy of cancer by trifunctional bacterium-based nanozymes. *ACS nano*. 2021;15 (12):19321–19333.
51. Kuo W-S, Wu C-M, Yang Z-S, et al.Biocompatible Bacteria@Au composites for application in the photothermal destruction of cancer cells. *Chem Commun*. 2008;(37):4430–4432. doi:10.1039/b808871c
52. Liu Y, Zhang M, Wang X, et al. Dressing bacteria with a hybrid immunoactive nanosurface to elicit dual anticancer and antiviral immunity. *Adv Mater*. 2023;35(11):e2210949. PMID: 36564893. doi:10.1002/adma.202210949
53. Wang L, Cao Z, Zhang M, Lin S, Liu J. Spatiotemporally controllable distribution of combination therapeutics in solid tumors by dually modified bacteria. *Adv Mater*. 2022;34(1):e2106669. PMID: 34687102. doi:10.1002/adma.202106669
54. Tu J, Xu H, Ma L, et al. Nintedanib enhances the efficacy of PD-L1 blockade by upregulating MHC-I and PD-L1 expression in tumor cells. *Theranostics*. 2022;12(2):747–766. PMID: 34976211; PMCID: PMC8692903. doi:10.7150/thno.65828
55. Thorn CF, Oshiro C, Marsh S, et al. Doxorubicin pathways: pharmacodynamics and adverse effects. *Pharmacogenet Genom*. 2011;21(7):440–446. doi:10.1097/FPC.0b013e32833ffb56
56. Park M, Lim J, Lee S, Nah Y, Kang Y, Kim WJ. Nanoparticle-mediated explosive anti-PD-L1 factory built in tumor for advanced immunotherapy. *Adv Mater*. 2025;37(7):e2417735. PMID: 39745112. doi:10.1002/adma.202417735
57. Caratelli S, De Paolis F, Silvestris DA, et al. The CD64/CD28/CD3ζ chimeric receptor reprograms T-cell metabolism and promotes T-cell persistence and immune functions while triggering antibody-independent and antibody-dependent cytotoxicity. *Exp Hematol Oncol*. 2025;14 (1):17. PMID: 39962623; PMCID: PMC11834217. doi:10.1186/s40164-025-00601-2
58. Chen R, Kang Z, Li W, et al. Extracellular vesicle surface display of αPD-L1 and αCD3 antibodies via engineered late domain-based scaffold to activate T-cell anti-tumor immunity. *J Extracell Vesicles*. 2024;13(7):e12490. PMID: 39051742; PMCID: PMC11270581. doi:10.1002/jev2.12490